



OPEN Topological transitions, pinning and ratchets for driven magnetic hopfions in nanostructures

J. C. Bellizotti Souza^{1✉}, C. J. O. Reichhardt², C. Reichhardt², A. Saxena², N. P. Vizarim³ & P. A. Venegas⁴

Using atomistic simulations, we examine the dynamics of three-dimensional magnetic hopfions interacting with an array of line defects or posts as a function of defect spacing, defect strength, and current. We find a pinned phase, a sliding phase where a hopfion can move through the posts or hurdles by distorting, and a regime where the hopfion becomes compressed and transforms into a toron that is half the size of the hopfion and moves at a lower velocity. The toron states occur when the defects are strong; however, in the toron regime, it is possible to stabilize sliding hopfions by increasing the applied current. Hopfions move without a Hall angle, while the toron moves with a finite Hall angle. We also show that when a hopfion interacts with an asymmetric array of planar defects, a ratchet effect consisting of a net dc motion can be realized under purely ac driving.

Keywords Hopfions, Stability, Ratchet

There has been growing interest in particle-like magnetic textures such as skyrmions, since an increasing number of systems are being found that can support these textured states^{1–5}. In addition to magnetic skyrmions, a variety of other textures can appear, such as antiskyrmions⁶ skyrmioniums⁷, antiferromagnetic skyrmions⁸, merons⁹, and biskyrmions^{10,11}. These textures can be manipulated or set into motion with applied currents^{12–14} or thermal gradients^{15,16}. Moving skyrmions can also interact with pinning sites, and their motion can be controlled by nanostructured patterns^{17,18}. Due to their size and stability, magnetic textures are promising candidates for various applications such as memory^{19–21} and novel computing approaches^{22,23}. These systems are also interesting in terms of basic science as they represent another particle-like system that can exhibit depinning phenomena^{18,24}, various sliding phases^{12,13,25}, melting²⁶, and rectification effects^{27,28}. In some cases, particularly for skyrmions, the textures have a strong non-dissipative Magnus term in their dynamics and move with a Hall angle θ with respect to an external drive^{29,30}. The Magnus force also affects how such textures interact with defects in the sample^{18,31}.

An example of particle-like textures that occur in three dimensions is hopfions^{32,33}, which are characterized by their Hopf index^{34,35}. In condensed matter systems, hopfions have been studied in liquid crystals^{36–38}, ferroelectrics³⁹, and magnetic systems^{40–49}. Ring type hopfions have recently been experimentally observed in magnetic systems⁵⁰. Due to their particle-like nature and their ability to be manipulated with external fields^{46,51–53}, hopfions are another promising system for applications, and could exhibit new kinds of dynamical effects when interacting with quenched disorder. Almost nothing is known, however, about how hopfions interact with quenched disorder or nanostructured arrays, how stable they are in such a system, and whether they can exhibit pinning and depinning behaviors or undergo topological transitions when driven through a nanostructured defect array.

In this work, we consider atomistic simulations of three-dimensional (3D) magnetic hopfions interacting with a comb-like array of line defects where the hopfions are driven through the defects under an applied current. We vary the spacing between the defects and modify the defect strengths by changing the local anisotropy. A hopfion subjected to an applied current moves without a Hall angle. When the hopfion interacts with the defects, we find a pinned regime where the hopfion cannot move between the defects, and a sliding regime where the hopfion can distort and slip between the defects. For strong disorder or dense defect arrays, we also find a regime in which the hopfion becomes so strongly compressed as it passes between the defects that it transforms to a toron

¹POSMAT-Programa de Pós-Graduação em Ciência e Tecnologia de Materiais, School of Sciences, São Paulo State University (UNESP), Bauru, São Paulo 17033-360, Brazil. ²Theoretical Division and Center for Nonlinear Studies, Los Alamos National Laboratory, Los Alamos, NM 87545, USA. ³Gleb Wataghin Institute of Physics, University of Campinas, Campinas, São Paulo 13083-859, Brazil. ⁴Department of Physics, School of Sciences, São Paulo State University (UNESP), Bauru, São Paulo 17033-360, Brazil. ✉email: jc.souza@unesp.br

that has a zero Hopf index^{44,54–56}. The toron is half as wide as the hopfion, moves at a slower velocity, and has a finite Hall angle. We find that in the regime where a toron forms just above depinning, if we apply a drive that is well above the depinning threshold, it is possible to stabilize a moving hopfion since the distortions experienced by the hopfion from the defect sites are reduced at higher drives. We also show that when a hopfion interacts with an asymmetric array of planar defects under a circular ac drive, a hopfion ratchet can be realized in which dc motion occurs where the hopfion translates by one substrate lattice site per ac drive cycle along the easy direction of the array asymmetry. Our results indicate that hopfion pinning and motion can be realized and controlled with nanostructured arrays, opening the possibility of a variety of applications that can be both similar to and different from those proposed for skyrmions.

Methods

Using atomistic simulations, we model a 3D chiral magnet sample of dimensions 128 nm × 128 nm × 17 nm with periodic boundary conditions along the x and y directions at zero temperature, $T = 0$ K. The 3D sample is modeled as a cubic arrangement of atoms, with lattice constant $a = 0.5$ nm. The Hamiltonian governing the atomistic simulations is given by^{13,57,58}:

$$\mathcal{H} = - \sum_{i, \langle i, j \rangle} J_{ij} \mathbf{m}_i \cdot \mathbf{m}_j - \sum_{i, \langle i, j \rangle} \mathbf{D}_{ij} \cdot (\mathbf{m}_i \times \mathbf{m}_j) - \sum_{i \in V} K_V (\mathbf{m}_i \cdot \hat{\mathbf{z}})^2 - \sum_{i \in T, B} K_S (\mathbf{m}_i \cdot \hat{\mathbf{z}})^2. \quad (1)$$

The first term is the exchange interaction between first neighbors, with exchange constant $J_{ij} = J$ between any two magnetic moments. The second term is the Dzyaloshinskii-Moriya (DM) interaction, where $\mathbf{D}_{ij} = D \hat{\mathbf{r}}_{ij}$ is the DM vector, D is the DM strength, and $\hat{\mathbf{r}}_{ij}$ is the unit distance vector between atomic moments i and j . This isotropic DM vector stabilizes Bloch hopfions, which have finite chirality. The third and fourth terms are perpendicular magnetic anisotropies (PMA), where V is the sample volume and T, B the sample top and bottom, respectively. Magnetic hopfions that form in a chiral magnetic background require confinement in order to remain stable⁵⁹, and therefore we impose $K_S \gg K_V$. Although our sample is 17 nm thick, the confinement reduces the effective thickness to 16 nm.

The time evolution of the magnetic moments is given by^{60,61}:

$$\frac{d\mathbf{m}_i}{dt} = -\gamma \mathbf{m}_i \times \mathbf{H}_i^{\text{eff}} + \alpha \mathbf{m}_i \times \frac{d\mathbf{m}_i}{dt} + \frac{j\hbar\gamma P a^3}{2ed\mu} \mathbf{m}_i \times (\hat{\mathbf{z}} \times \hat{\mathbf{j}}) \times \mathbf{m}_i. \quad (2)$$

Here γ is the electron gyromagnetic ratio, $\mathbf{H}_i^{\text{eff}} = -\frac{1}{\mu} \frac{\partial \mathcal{H}}{\partial \mathbf{m}_i}$ is the effective field, $\mu = \hbar\gamma$ is the atomic magnetic moment, α is the phenomenological Gilbert damping, and the last term is the spin orbit torque (SOT) contribution, where j is the current density, $P = 1$ is the current polarization, e is the electron charge, $d = 17$ nm is the film thickness and $\hat{\mathbf{j}}$ is the current direction.

The hopfion is characterized by the Hopf index^{33–35}, given by:

$$Q_H = \int_V \mathbf{B} \cdot \mathbf{A} \, d^3x, \quad (3)$$

where the integration is performed over the whole sample. Here \mathbf{B} is the emergent magnetic field and \mathbf{A} is the corresponding vector potential, $\mathbf{B} = \nabla \times \mathbf{A}$. The unitless emergent magnetic field can be computed using $B_i = \frac{1}{8\pi} \varepsilon_{ijk} \mathbf{m} \cdot (\partial_j \mathbf{m} \times \partial_k \mathbf{m})$; however, better numerical results are obtained when using a lattice based approach⁴⁸, which is the method we employ throughout this work. The vector potential \mathbf{A} used in the Hopf index computation is given by:

$$A_x(x, y, z) = \int_0^y B_z(x, l, z) \, dl, \quad (4)$$

$$A_y(x, y, z) = 0, \quad (5)$$

$$A_z(x, y, z) = - \int_0^y B_x(x, l, z) \, dl, \quad (6)$$

which is known to give good Hopf index computation results⁴⁸.

We integrate Eq. (2) using a fourth order Runge–Kutta integration method over a time span of 60 ns when considering the topological transitions, and over 360 ns when considering ratchet effects. Our simulations have a fixed integration time step of $\Delta t = 0.01\hbar/J$.

In previous work on chiral magnetic hopfions, the dynamics were integrated over a time span of 15 ns; however, here we are focusing on topological transitions and ratchet effects, and therefore require longer simulation times.

Our sample has parameters $J = 1$ meV, $D = 0.2J$, $K_V = 0.01J$, and $K_{T, B} = 5J$. These parameters roughly correspond to the magnetic parameters of the chiral magnet MnSi^{13,58,59}. Although we use normalized values of D , K_V and $K_{T, B}$, the unnormalized values can be obtained by multiplying the constants by J ; this gives $D = 0.2$ meV, $K_V = 0.01$ meV and $K_{T, B} = 5$ meV.

To ensure the stability of the hopfion, we first used the ansatz presented in Knapman et al.⁴⁸ and performed a 60 ns integration with no SOT. This integration gives a final \mathbf{m} configuration that we then employed as the initial condition for our simulations.

Results

We consider a $Q_H = 1$ 3D hopfion driven through a comb-like array of line defects that have a higher value of K_D than the surrounding medium. In Fig. 1a, we show a 3D rendering of the $m_z = 0$ isosurface for the hopfion. The inset shows the $m_x = 1$ and $m_x = -1$ isosurfaces, highlighting the knot-like structure that is characteristic of a hopfion with $Q_H = 1$. A side view and a top view of the hopfion appear in Fig 1b, c, respectively. In this case, the hopfion diameter is approximately 25 nm. Arrows in Fig. 1a indicate the direction of the applied current j as well as the direction \mathbf{v} along which the hopfion moves. The two black pillars are the columnar line defects, which are placed a distance Δ apart. For different values of j , Δ , and K_D , we apply the current and wait for the system to evolve to a pinned or sliding state or to transform into a toron when the hopfion moves between the defects. Due to the confinement inside the sample, the hopfion motion in the absence of the line defects is similar to what was observed previously in Ref. ⁵⁹, where the hopfion moves without a Hall angle.

As a function of changing drive and defect parameters, we find three phases: (i) a pinned phase where the current is so low that the hopfion cannot move between the line defects and is pinned between them, (ii) a sliding phase where the hopfion can distort and pass between the defects, and (iii) a regime where the hopfion becomes so strongly compressed upon moving between the defects that it transforms into a dipolar string state or a toron^{54,62} with $Q_H = 0$, as shown in Fig. 2a. Here, the ring-like structure associated with the $Q_H = 1$ hopfion in Fig. 1 is missing, and the plot of the $m_x = 1$ and $m_x = -1$ isosurfaces in the inset of Fig. 2 indicate that there is no knotting. The yz or side view cross-section and the xy or top view cross-section of the toron appear in Fig. 2b, c, respectively. The toron is close to $\xi = 12$ nm in diameter, approximately half the size of the hopfion.

In Fig. 3a, we plot a phase diagram as a function of the defect spacing Δ versus current j in a system with a defect strength of $K_D = 5J$. We find a pinned phase, sliding motion of the hopfion between the defects, and a phase in which the $Q_H = 1$ hopfion undergoes a topological transition to a $Q_H = 0$ toron. The width of the pinned phase grows with decreasing Δ . When $\Delta > 23$ nm, the hopfion can depin into a moving hopfion as the current increases. Since the hopfion diameter is about 24 nm, the distortions induced in the hopfion by the defects as it passes between them are reduced when $\Delta > 23$ nm. For $\Delta < 23$ nm, we find a pinned phase and a toron state; however, when j is sufficiently large, the hopfion moves between the defects so rapidly that it does not deform strongly enough to transform into a toron, and the moving hopfion phase reappears. In previous

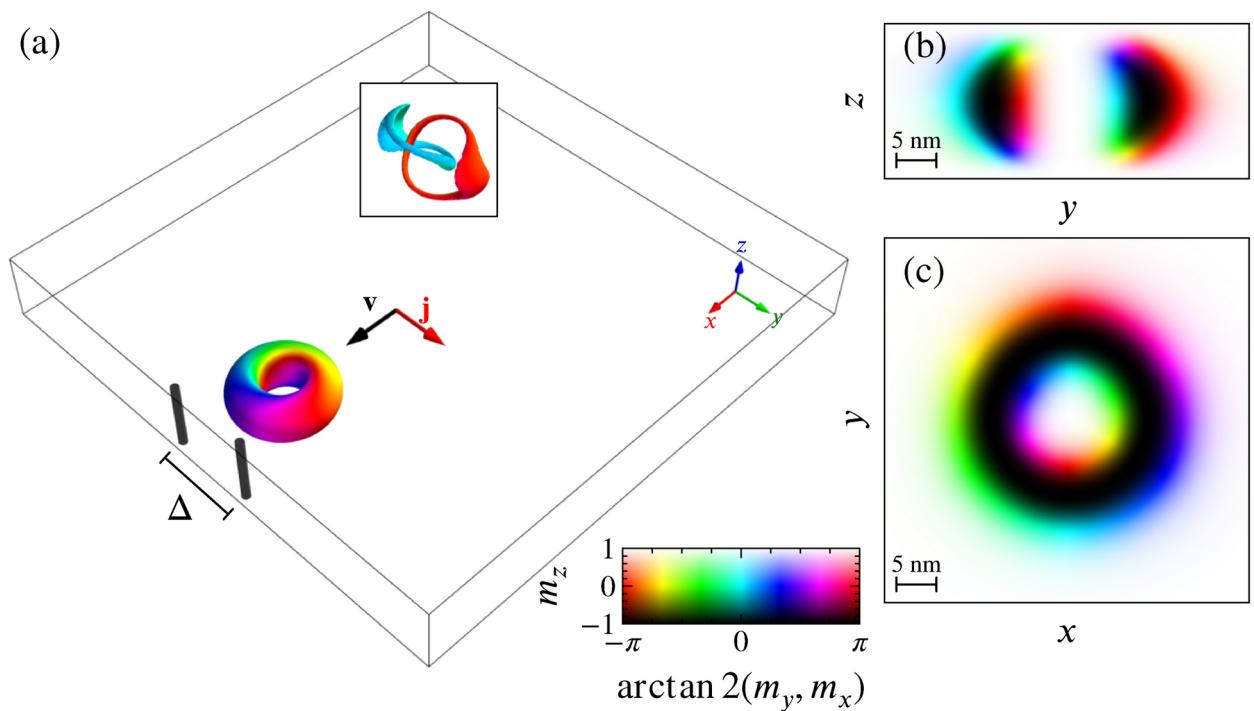


Fig. 1. (a) 3D view of our system for a $Q_H = 1$ hopfion, which is plotted by visualizing the $m_z = 0$ isosurface. The colors represent the m direction given by the angle between m_x and m_y , as shown in the colorbar. We place two column-like defects (thick black lines) with an increased PMA of K_D , where Δ is the distance between the two columns. The hopfion is subjected to dc driving along \hat{y} produced by a current j . This moves the hopfion along $\hat{v} = \hat{x}$ at a velocity v towards the center point between the two columns. Inset: hopfion isosurfaces at $m_x = 1$ (red) and $m_x = -1$ (cyan). (b) zy and (c) xy cross-sections along the hopfion center. The hopfion has a diameter of approximately $\xi = 25$ nm.

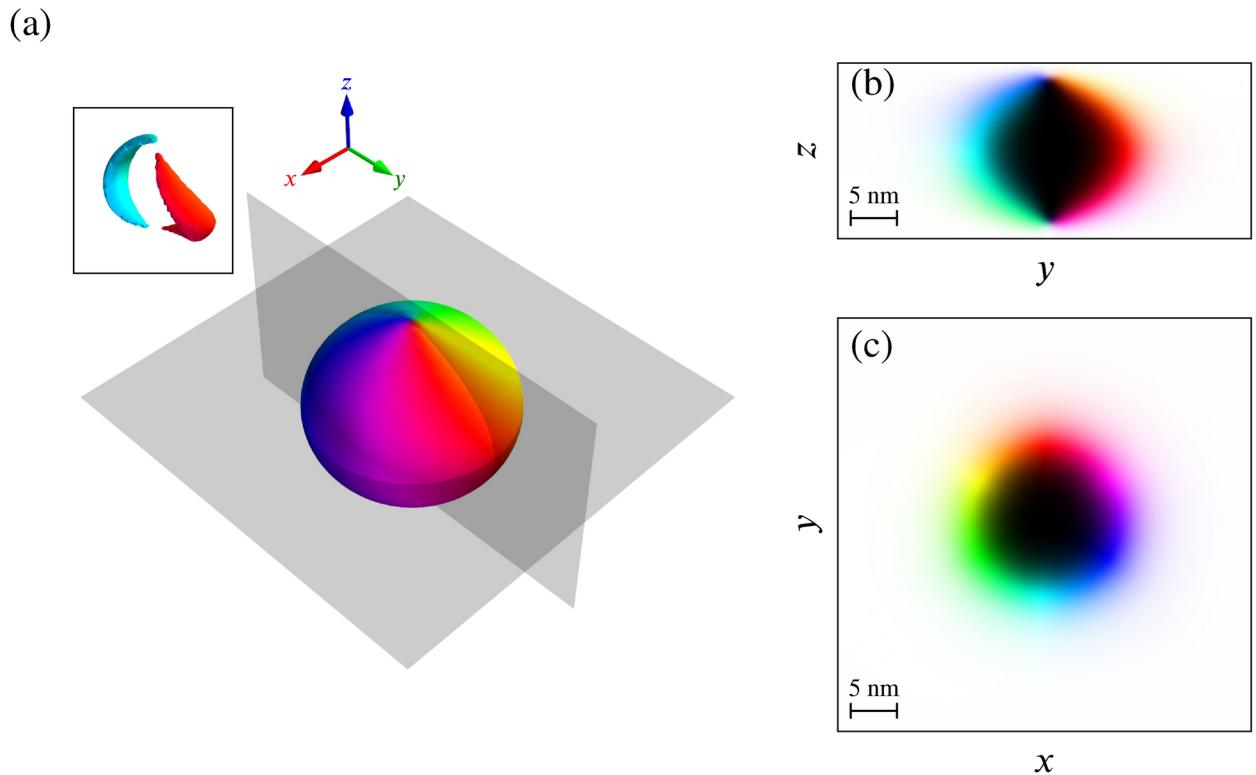


Fig. 2. (a) Isosurface of $m_z = 0$ showing a dipole string texture or a toron with $Q_H = 0$. The hopfion topologically transitions to the toron texture for certain combinations of Δ , K_D and j . Inset: the $m_x = 1$ (red) and $m_x = -1$ (cyan) isosurfaces. (b) zy , (c) xy cross-sections along the dipole string center. The dipole string diameter is approximately $\xi = 12$ nm. The colors represent the \mathbf{m} direction, with the color given by the angle between m_y and m_x , and the brightness given by the m_z value, following the colormap presented in Fig. 1.

work on systems with depinning, it has been shown that the distortions produced by the pinning on the moving textures is effectively reduced at higher drives⁶³, and this effect has been studied for skyrmions in both particle based²⁵ and continuum models⁶⁴.

The ability of the defects to transform the hopfion to a toron is affected by the defect strength. In Fig. 3b we present a phase diagram as a function of K_D/J versus j for fixed $\Delta = 21$ nm, which is smaller than the hopfion width. For $K_D < 1.3$ J the hopfion can depin into a moving hopfion state, while for $K_D > 1.3$ J the hopfion transforms into a toron upon depinning, and a larger j must be applied in order to stabilize a moving hopfion.

The transition from a pinned phase to a moving hopfion phase at fixed j and varying Δ is a consequence of the finite size of the hopfion. When the spacing between the defects is not large enough, the hopfion cannot move through the defects and stays pinned. Increasing the spacing enables the hopfion to move through the defects without transitioning to a toron, since the hopfion now weakly interacts with the defects. At higher currents, the hopfion still cannot move through the defects, but now the current is strong enough to induce a transition from a hopfion to a toron. In this case, when the defect spacing is increased and the interaction between the hopfion and the defects is reduced, the phase transition is from a toron to a moving hopfion. Alternatively, by fixing Δ and varying j , the same phase transitions appear, but now the transitions are a consequence of the applied driving force and the time the hopfion spends interacting with the defects, which changes as a function of the driving current. The phase transitions are different when j is fixed and K_D is varied. At low j , a moving hopfion transitions to a pinned hopfion with increasing K_D . Although the defect spacing is fixed in this case, the hopfion interacts more strongly with the defects at higher K_D , which in turn makes it more difficult for the hopfion to move through the defects. At higher values of j , the transition is from a moving hopfion to a toron, and this is again a consequence of the hopfion interacting more strongly with defects that have higher K_D .

It would be possible to construct a phase diagram as a function of K_D versus Δ for fixed values of j . A moving hopfion phase would appear when K_D is smaller than a critical value. When K_D is above this critical value and Δ is also larger than the hopfion diameter, a moving hopfion phase should also be present. Intermediate values of K_D and Δ would produce the three phases we observe in Fig. 3. The range of K_D and Δ values over which each phase would appear would depend on whether the hopfion can move through the defects, which is determined by a competition between K_D , Δ , and j .

The phase diagram in Fig. 3 was constructed based on the value of Q_H and the average texture velocity. The texture velocity is computed in a texture independent manner by using a DBSCAN algorithm⁶⁵, modified to find varying m_z textures, that determines the x , y , and z position coordinates of the texture. We then obtain the

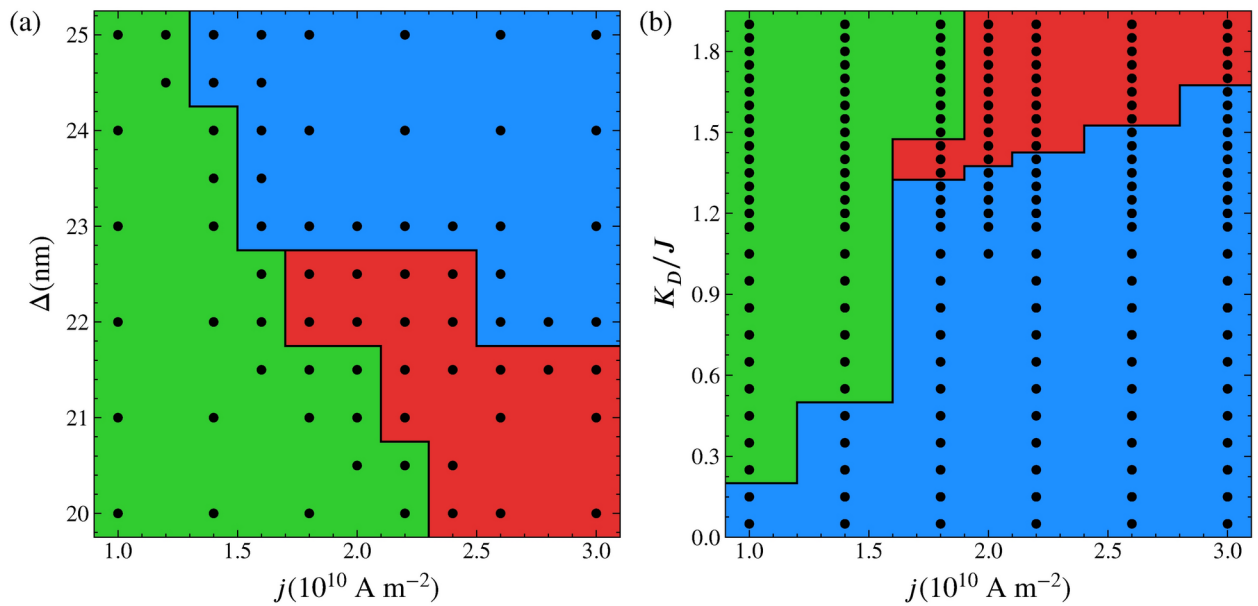


Fig. 3. Phase diagrams for a hopfion interacting with a line defect structure as in Fig. 1a, showing a pinned state (green), hopfion motion between the defects (blue), and a topological transition from a $Q_H = 1$ hopfion to an unlinked $Q_H = 0$ toron $Q_H = 0$ (red). (a) Phases as a function of the spacing between the two columns Δ vs current j for a defect strength of $K_D = 5J$. (b) Phases as a function of the defect strength K_D/J vs current j for a defect spacing of $\Delta = 21$ nm. The black dots indicate the points at which simulation data was obtained.

velocity by computing central differences of the positions from frame to frame of the simulation. If $Q_H = 1$ is not satisfied, we classify the phase as containing a topological transition; similarly, if the velocity $\langle v \rangle \approx 0$ we classify the phase as a pinned phase.

In Fig. 4, we illustrate the pinning-induced transition of the hopfion into a toron for the system from Fig. 3a at $\Delta = 21$ nm, $K_D = 5J$, and $j = 2.6 \times 10^{10}$ A m⁻². Figure 4a–d shows 3D images of the $m_z = 0$ isosurface of the texture along with the defect positions, while Fig. 4e–h shows the side view and Fig. 4i–l shows the top view of the texture. As the hopfion moves between the line defects, it becomes increasingly compressed, and at $t = 26$ ns, it collapses into the $Q_H = 0$ state. The images also show that the toron is smaller than the hopfion. The line defects are modeled as columns of sites with high anisotropy, which locks the magnetic moments composing the defect into the easy axis direction. In the case of weak anisotropy defects, the magnetic moments composing the defect are not locked, but instead have a weak tendency to align along the easy axis direction, which can affect the configuration of the line defect. In most of our systems, such as those shown in Fig. 4, the defect anisotropy is high enough so that the magnetic moments are indeed locked. An exception is the systems in Fig. 3b, where the defect anisotropy strength varies.

In Fig. 5a–d, we show the top view of a moving hopfion at $j = 2.6 \times 10^{10}$ A m⁻² in the sample from Fig. 4 where a hopfion to toron transition occurs. In the images, the hopfion is not close to the columnar defects and is not affected by them. The hopfion moves at a velocity $v = 2.7$ m s⁻¹, without a Hall angle. Figure 5e–h shows the top view of the moving toron away from the columnar defects after the transition. The toron travels at a velocity of $v = 1.1$ m s⁻¹ with a Hall angle of approximately $\theta = 43^\circ$.

In Fig. 6, we show the displacements Δx (black) and Δy (red) versus time for the system in Fig. 4 with $j = 2.6 \times 10^{10}$ A m⁻², $\Delta = 21$ nm, and $K_D = 5J$, where the hopfion transforms to a toron near $t = 28$ ns upon interacting with the line defects. The hopfion moves with a higher velocity of $v = 2.7$ m s⁻¹, visible as the larger slope in Δx , while $\Delta y = 0.0$ for the hopfion, indicating that there is no Hall angle. When the hopfion begins to interact with the defects near $t = 20$ ns, there is a dip in Δx as the texture slows down. After the transition, the toron moves at $v = 1.1$ m s⁻¹ with a Hall angle of $\theta = 43^\circ$, which appears as the onset of finite Δy and a reduced slope of Δx . In Fig. 6b we plot the corresponding Hopf index Q_H versus time. For $t < 28$ ns, $Q_H = 1$ and a hopfion is present, while at later times, Q_H drops in the toron state. The oscillations in Q_H that appear after the transition are numerical artifacts. The hopfion is a stable object in the absence of driving and pinning, so the topological transition in Fig. 6b does not occur spontaneously. Instead, the transition to a toron is induced by the interaction of the hopfion with the line defects, and this interaction is itself caused by the application of a driving force which pushes the hopfion against the defects.

Since the line defects are able to pin the hopfion, this suggests that certain types of defects could also guide the hopfion motion. In addition, if an asymmetric arrangement of defects were introduced, the system could exhibit a ratchet effect. In a rocking ratchet, an ac drive applied to a particle on an asymmetric substrate produces a net dc drift motion. Rocking ratchets have been realized for overdamped superconducting vortices interacting with asymmetric substrates under ac driving^{66–71}. Ratchet effects have also been observed for skyrmions interacting

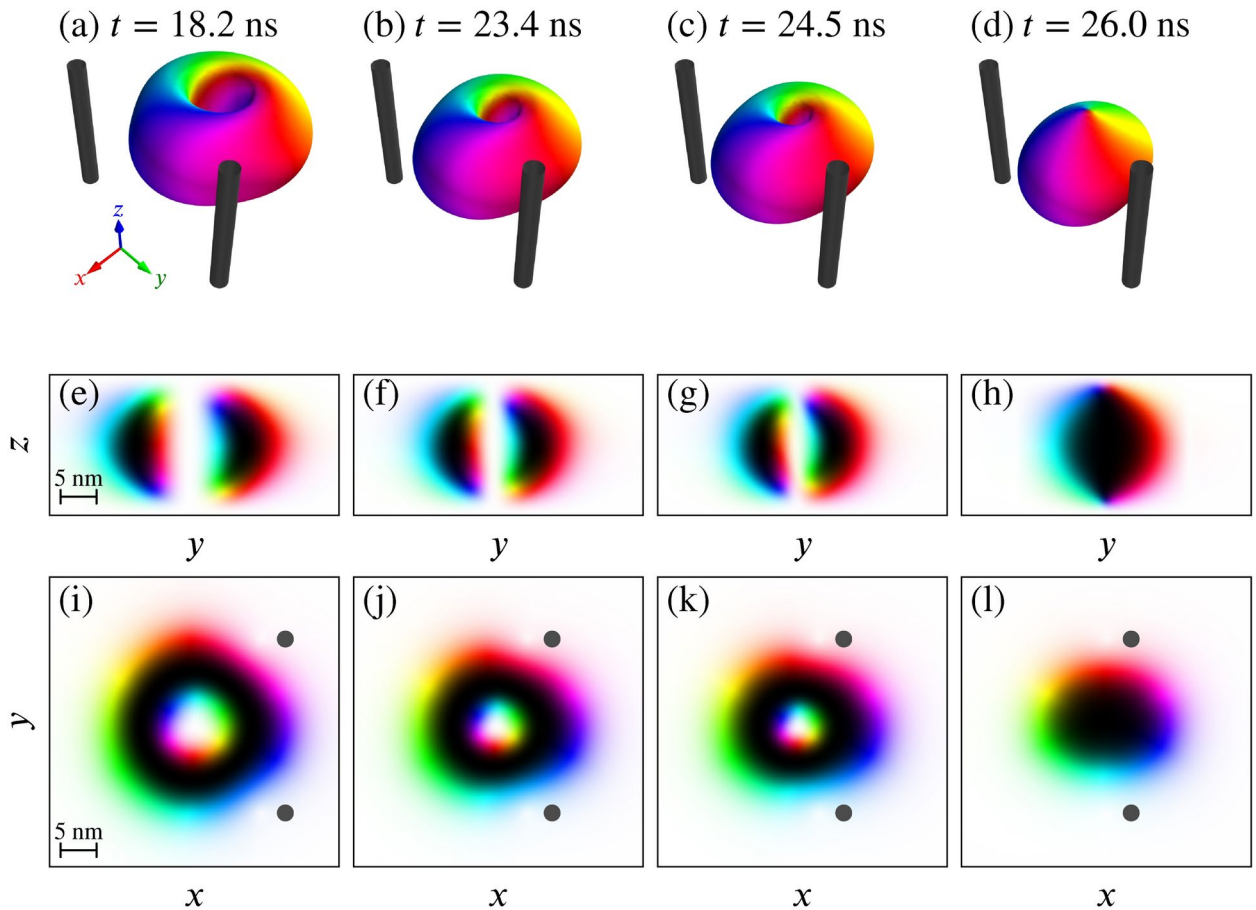


Fig. 4. Images of a hopfion topologically transitioning from $Q_H = 1$ to $Q_H = 0$ upon interacting with the columnar defects. Here $\Delta = 21$ nm and $j = 2.6 \times 10^{10}$ A m $^{-2}$. **(a,b,c,d)** $m_z = 0$ isosurfaces. **(e,f,g,h)** The yz cross-section. **(i,j,k,l)** The xy cross-section. The scale bar in panel **(e)** applies to panels **(e, f, g, h)**, while the scale bar in panel **(i)** applies to panels **(i, j, k, l)**. The colors represent the \mathbf{m} direction, with the color given by the angle between m_y and m_x , and the brightness given by the m_z value, following the colormap presented in Fig. 1.

with asymmetric substrates; however, in the skyrmion system, the Magnus force provides additional ways for the texture to be rectified^{27,28,72}. Since hopfions do not have a Hall angle, their ratcheting motion would be expected to be comparable to that of the overdamped superconducting vortex systems. A hopfion ratchet would then represent a realization of a ratchet for a 3D object.

In Fig. 7a we show a top view of a substrate containing a herringbone planar defect array with anisotropy of $K_D = 0.5J$. We place a hopfion in the center region near $x = 75$ nm and apply a circular ac drive given by $\mathbf{j}_{AC} = j_{AC} \sin(2\pi ft)\hat{x} - j_{AC} \cos(2\pi ft)\hat{y}$, with $j_{AC} = 2 \times 10^{10}$ A m $^{-2}$ and frequency $f = 0.01$ GHz. The lines show the hopfion trajectory, where we change the color for each successive ac cycle to show that the hopfion is translating along the negative x -direction corresponding to the easy flow direction of the substrate asymmetry. Figure 7b shows the hopfion velocity v_x and v_y versus time for the system in Fig. 7a. The texture translates by one substrate lattice site per cycle in the negative x direction. In this case, we must apply a circular ac drive in order to break enough symmetry to obtain a ratchet effect; however, the finite Magnus force of the toron could produce an additional circular motion so that an ac drive applied along only one axis could be sufficient to produce ratchet transport. Other defect geometries could permit the ratcheting motion of the hopfions under uniaxial ac driving.

Discussion

Our results indicate that hopfions can interact with and be controlled by structured defect arrays. We considered defects created by varying the perpendicular magnetic anisotropy; however, defects could be also generated by varying other parameters of the sample. The line defects we study could be fabricated by a variety of irradiation techniques, such as a focused ion beam pattern. Alternatively, the surface could be patterned with magnetic dots or via surface etching. Although we studied only a single hopfion, we expect that additional dynamical behaviors could arise for multiply interacting hopfions or for hopfions with higher Hopf indices, where there could be transitions from higher to lower indices. We found that the hopfion transforms to the dipolar string texture

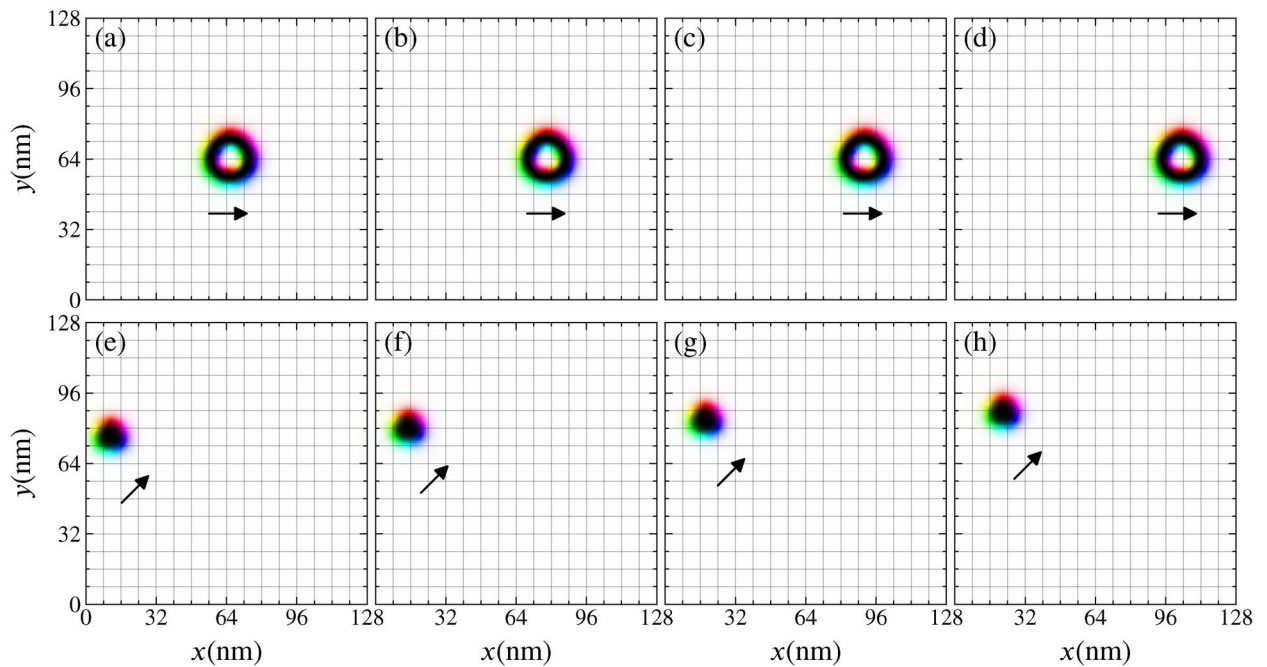


Fig. 5. Images of freely moving textures away from the influence of the defect lines in the system from Fig. 4 with $\Delta = 21$ nm and $j = 2.6 \times 10^{10}$ A m $^{-2}$ where a hopfion to toron transformation occurs. (a–d) Hopfion motion, with no Hall angle, $\theta = 0^\circ$, before the transformation at (a) $t = 0$ ns, (b) $t = 5.1$ ns, (c) $t = 9.6$ ns, and (d) $t = 14.1$ ns. (e–h) Dipole string, or toron, motion, with a Hall angle of $\theta = 43^\circ$ after the transformation at (e) $t = 40.8$ ns, (f) $t = 45.3$ ns, (g) $t = 49.8$ ns, and (h) $t = 54.3$ ns. The velocity of the hopfion is roughly $v = 2.7$ m s $^{-1}$, and that of the dipole string is roughly $v = 1.1$ m s $^{-1}$. Arrows indicate the direction of motion. The colors represent the \mathbf{m} direction, with the color given by the angle between m_y and m_x , and the brightness given by the m_z value, following the colormap presented in Fig. 1.

upon interacting with defects, but it would also be interesting to see if the reverse transformation could occur, or if a nanostructured pattern could be used to nucleate hopfions in a controlled fashion. In our system, the hopfions are confined, and most experiments with line defects would likely fall into the same type of confined geometry, but it would also be interesting to study hopfion dynamics in bulk systems where it is known that there can be additional 3D dynamics⁴⁴. We also considered only line-like and planar defects, but surface defects or defects in the bulk would also be interesting to explore. This topological transition is akin to that observed for a skyrmionium turning into a skyrmion upon passing through a constriction.

We note that Wang et al.⁵⁹ addressed the dynamics of Néel hopfions in the presence of currents that produce both spin Hall torques and spin-transfer torques in a clean racetrack. Here we consider the dynamics of a Bloch hopfion under currents that produce spin Hall torques which, according to Ref. ⁵⁹, have a driving force perpendicular to the current, rather than parallel to the current as is the case for Néel hopfions. We find two distinct results regarding hopfion dynamics that do not appear in Ref. ⁵⁹: (i) the topological transition from a hopfion to a toron produced by interactions with anisotropy defects and currents, and (ii) the ratchet effect of a hopfion under circular ac driving interacting with an asymmetric array of defects.

Conclusion

Using atomistic simulations, we have examined the dynamics of driven hopfions interacting with line-like defects. As we vary the driving, the distance between the defects, and the defect disorder strengths, we find three phases: a pinned state, a sliding hopfion phase where there is a critical depinning drive and the hopfions can move between the defects by distorting, and a state where the hopfion transforms into a dipolar string or toron that is half the size of the hopfion and moves at a lower velocity for the same applied current. For disorder strengths and defect spacings at which the hopfion transforms into a toron at depinning, we find that if the drive is increased sufficiently far above the depinning transition, a moving hopfion can be stabilized. The hopfion moves without a Hall angle, but the toron moves with a finite Hall angle. When we introduce asymmetric arrays of planar defects, a hopfion ratchet effect can be realized under circular ac driving. Our results suggest that the position and dynamics of hopfions can be controlled with judiciously constructed defect arrays. This opens the possibility of a variety of applications utilizing hopfions, such as memory elements or new types of computing devices. In addition to magnetic textures, our results are also relevant to hopfions in ferroelectrics or in liquid systems under fluid flow conditions.

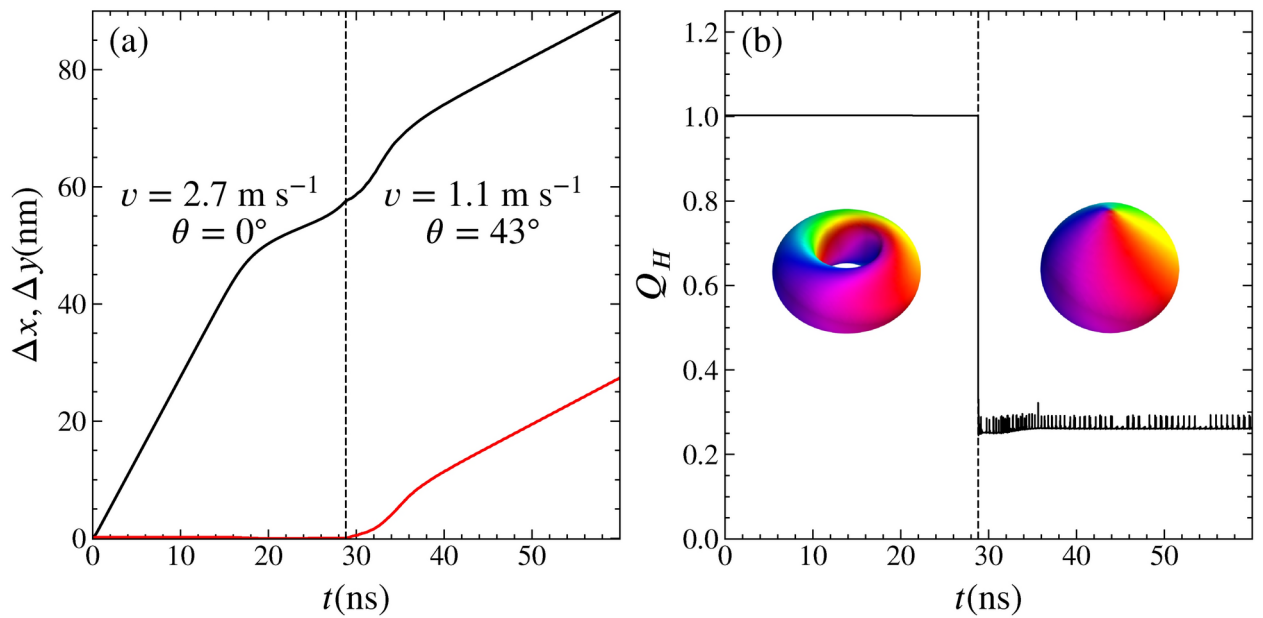


Fig. 6. (a) Displacements Δx (black) and Δy (red) versus time for the system from Fig. 4 with $j = 2.6 \times 10^{10} \text{ A m}^{-2}$, $\Delta = 21 \text{ nm}$, and $K_D = 5J$, where a transition from a hopfion to a toron occurs as the hopfion passes between the defects. The hopfion travels at a higher velocity of $v = 2.7 \text{ m s}^{-1}$ and with no Hall angle, whereas the dipole string moves at a slower velocity of $v = 1.1 \text{ m s}^{-1}$ with a Hall angle of $\theta = 43^\circ$. (b) The corresponding Hopf index Q_H versus time. The oscillations in Q_H that appear after the transition are numerical artifacts. In each panel, a dashed line marks the moment at which the hopfion to toron transition occurs. The colors in the insets of (b) represent the \mathbf{m} direction, with the color given by the angle between m_y and m_x , and the brightness given by the m_z value, following the colormap presented in Fig. 1. The 3D axis of the insets in (b) are the same as the ones in Figs. 1, 2, and 4a–d.

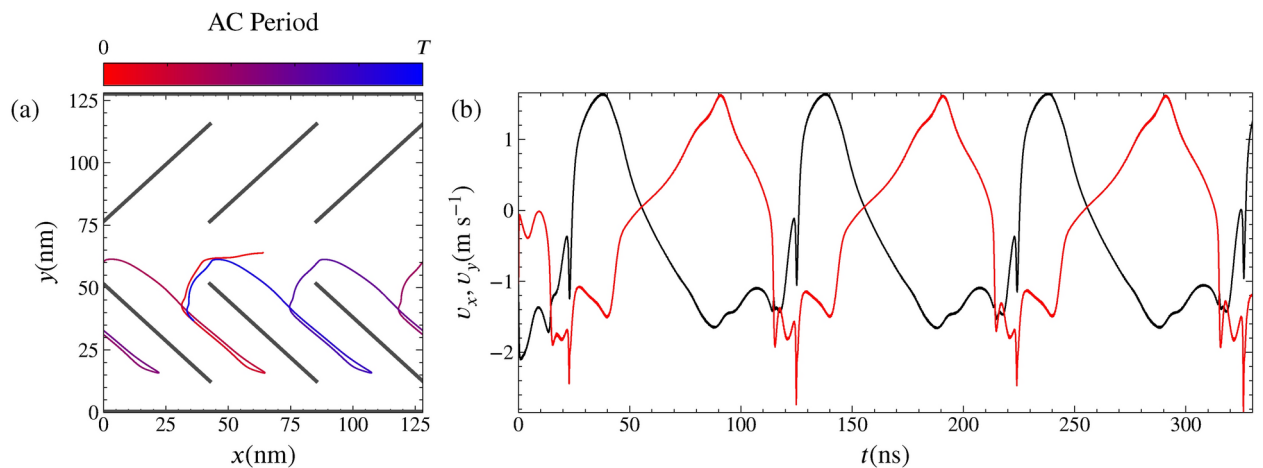


Fig. 7. (a) Image of the trajectory of a hopfion, colored according to the progression of the circular ac driving period, moving through a herringbone planar defect array pattern (gray lines) in a sample with $K_D = 0.5J$. (b) The hopfion velocity v_x (black) and v_y (red) vs time for the system in (a). An animation showing the hopfion ratchet motion is available in the Supplemental Material (see supplemental material for animations showing the motion of the textures).

Data availability

Data is provided within the manuscript or supplementary information files.

Received: 31 January 2025; Accepted: 6 May 2025

Published online: 14 May 2025

References

- Mühlbauer, S. et al. Skyrmion lattice in a chiral magnet. *Science* **323**, 915–919. <https://doi.org/10.1126/science.1166767> (2009).
- Yu, X. Z. et al. Skyrmion flow near room temperature in an ultralow current density. *Nat. Commun.* **3**, 988. <https://doi.org/10.1038/ncomms1990> (2012).
- Nagaosa, N. & Tokura, Y. Topological properties and dynamics of magnetic skyrmions. *Nat. Nanotechnol.* **8**, 899–911. <https://doi.org/10.1038/NNANO.2013.243> (2013).
- Woo, S. et al. Observation of room-temperature magnetic skyrmions and their current-driven dynamics in ultrathin metallic ferromagnets. *Nat. Mater.* **15**, 501–506. <https://doi.org/10.1038/NMAT4593> (2016).
- Everschor-Sitte, K., Masell, J., Reeve, R. M. & Kläui, M. Perspective: Magnetic skyrmions—Overview of recent progress in an active research field. *J. Appl. Phys.* **124**, 240901. <https://doi.org/10.1063/1.5048972> (2018).
- Nayak, A. K. et al. Magnetic antiskyrmions above room temperature in tetragonal Heusler materials. *Nature (London)* **548**, 561–566. <https://doi.org/10.1038/nature23466> (2017).
- Kolesnikov, A. G., Stebliy, M. E., Samardak, A. S. & Ognev, A. V. Skyrmionium—High velocity without the skyrmion Hall effect. *Sci. Rep.* **8**, 16966. <https://doi.org/10.1038/s41598-018-34934-2> (2018).
- Jani, H. et al. Antiferromagnetic half-skyrmions and bimerons at room temperature. *Nature (London)* **590**, 74. <https://doi.org/10.1038/s41586-021-03219-6> (2021).
- Yu, X. Z. et al. Transformation between meron and skyrmion topological spin textures in a chiral magnet. *Nature (London)* **564**, 95–98. <https://doi.org/10.1038/s41586-018-0745-3> (2018).
- Yu, X. Z. et al. Biskyrmion states and their current-driven motion in a layered manganite. *Nat. Commun.* **5**, 3198. <https://doi.org/10.1038/ncomms4198> (2014).
- Göbel, B., Mertig, I. & Tretiakov, O. A. Beyond skyrmions: Review and perspectives of alternative magnetic quasiparticles. *Phys. Rep.* **895**, 1. <https://doi.org/10.1016/j.physrep.2020.10.001> (2021).
- Jonietz, F. et al. Spin transfer torques in MnSi at ultralow current densities. *Science* **330**, 1648–1651. <https://doi.org/10.1126/science.1195709> (2010).
- Iwasaki, J., Mochizuki, M. & Nagaosa, N. Current-induced skyrmion dynamics in constricted geometries. *Nat. Nanotechnol.* **8**, 742–747. <https://doi.org/10.1038/nnano.2013.176> (2013).
- Legrand, W. et al. Room-temperature current-induced generation and motion of sub-100 nm skyrmions. *Nano Lett.* **17**, 2703–2712. <https://doi.org/10.1021/acs.nanolett.7b00649> (2017).
- Mochizuki, M. et al. Thermally driven ratchet motion of a skyrmion microcrystal and topological magnon Hall effect. *Nat. Mater.* **13**, 241–246. <https://doi.org/10.1038/NMAT3862> (2014).
- Wang, Z. et al. Thermal generation, manipulation and thermoelectric detection of skyrmions. *Nat. Electron.* **3**, 672. <https://doi.org/10.1038/s41928-020-00489-2> (2020).
- Juge, R. et al. Helium ions put magnetic skyrmions on the track. *Nano Lett.* **21**, 2989–2996. <https://doi.org/10.1021/acs.nanolett.1c00136> (2021).
- Reichhardt, C., Reichhardt, C. J. O. & Milosevic, M. Statics and dynamics of skyrmions interacting with disorder and nanostructures. *Rev. Mod. Phys.* **94**, 035005. <https://doi.org/10.1103/RevModPhys.94.035005> (2022).
- Fert, A., Reyren, N. & Cros, V. Magnetic skyrmions: Advances in physics and potential applications. *Nat. Rev. Mater.* **2**, 17031. <https://doi.org/10.1038/natrevmats.2017.31> (2017).
- Finocchio, G., Büttner, F., Tomasello, R., Carpentieri, M. & Kläui, M. Magnetic skyrmions: From fundamental to applications. *J. Phys. D Appl. Phys.* **49**, 423001. <https://doi.org/10.1088/0022-3727/49/42/423001> (2016).
- Vakili, H. et al. Skyrmionics - computing and memory technologies based on topological excitations in magnets. *J. Appl. Phys.* **130**, 070908. <https://doi.org/10.1063/5.0046950> (2021).
- Pinna, D., Bourianoff, G. & Everschor-Sitte, K. Reservoir computing with random skyrmion textures. *Phys. Rev. Appl.* **14**, 054020. <https://doi.org/10.1103/PhysRevApplied.14.054020> (2020).
- Song, K. M. et al. Skyrmion-based artificial synapses for neuromorphic computing. *Nat. Electron.* **3**, 148–155. <https://doi.org/10.1038/s41928-020-0385-0> (2020).
- Lin, S.-Z., Reichhardt, C., Batista, C. D. & Saxena, A. Particle model for skyrmions in metallic chiral magnets: Dynamics, pinning, and creep. *Phys. Rev. B* **87**, 214419. <https://doi.org/10.1103/PhysRevB.87.214419> (2013).
- Reichhardt, C., Ray, D. & Reichhardt, C. J. O. Collective transport properties of driven skyrmions with random disorder. *Phys. Rev. Lett.* **114**, 217202. <https://doi.org/10.1103/PhysRevLett.114.217202> (2015).
- Huang, P. et al. Melting of a skyrmion lattice to a skyrmion liquid via a hexatic phase. *Nat. Nanotechnol.* **15**, 761. <https://doi.org/10.1038/s41565-020-0716-3> (2020).
- Göbel, B. & Mertig, I. Skyrmion ratchet propagation: Utilizing the skyrmion Hall effect in AC racetrack storage devices. *Sci. Rep.* **11**, 3020. <https://doi.org/10.1038/s41598-021-81992-0> (2021).
- Souza, J. C. B., Vizirim, N. P., Reichhardt, C. J. O., Reichhardt, C. & Venegas, P. A. Skyrmion ratchet in funnel geometries. *Phys. Rev. B* **104**, 054434. <https://doi.org/10.1103/PhysRevB.104.054434> (2021).
- Jiang, W. et al. Direct observation of the skyrmion Hall effect. *Nat. Phys.* **13**, 162–169. <https://doi.org/10.1038/NPHYS3883> (2017).
- Litzius, K. et al. Skyrmion Hall effect revealed by direct time-resolved X-ray microscopy. *Nat. Phys.* **13**, 170–175. <https://doi.org/10.1038/NPHYS4000> (2017).
- Zeissler, K. et al. Diameter-independent skyrmion Hall angle observed in chiral magnetic multilayers. *Nat. Commun.* **11**, 428. <https://doi.org/10.1038/s41467-019-14232-9> (2020).
- Faddeev, L. D. Some comments on the many-dimensional solitons. *Lett. Math. Phys.* **1**, 289–293. <https://doi.org/10.1007/BF00398483> (1976).
- Faddeev, L. & Niemi, A. J. Stable knot-like structures in classical field theory. *Nature (London)* **387**, 58. <https://doi.org/10.1038/387058a0> (1997).
- Hopf, H. Über die Abbildungen der dreidimensionalen Sphäre auf die Kugelfläche. *Math. Annal.* **104**, 637–665. <https://doi.org/10.1007/BF01457962> (1931).
- Whitehead, J. H. C. An expression of Hopf's invariant as an integral. *Proc. Natl. Acad. Sci. (USA)* **33**, 117–123. <https://doi.org/10.1073/pnas.33.5.117> (1947).
- Ackerman, P. J., Boyle, T. & Smalyukh, I. I. Squirming motion of baby skyrmions in nematic fluids. *Nat. Commun.* **8**, 673. <https://doi.org/10.1038/s41467-017-00659-5> (2017).
- Ackerman, P. J. & Smalyukh, I. I. Diversity of knot solitons in liquid crystals manifested by linking of preimages in torons and hopfions. *Phys. Rev. X* **7**, 011006. <https://doi.org/10.1103/PhysRevX.7.011006> (2017).
- Tai, J.-S.B., Ackerman, P. J. & Smalyukh, I. I. Topological transformations of Hopf solitons in chiral ferromagnets and liquid crystals. *Proc. Natl. Acad. Sci.* **115**, 921–926. <https://doi.org/10.1073/pnas.1716887115> (2018).
- Luk'yanchuk, I., Tikhonov, Y., Razumnaya, A. & Vinokur, V. M. Hopfions emerge in ferroelectrics. *Nat. Commun.* **11**, 2433. <https://doi.org/10.1038/s41467-020-16258-w> (2020).
- Sutcliffe, P. Hopfions in chiral magnets. *J. Phys. A Math. Theor.* **51**, 375401. <https://doi.org/10.1088/1751-8121/aad521> (2018).
- Tai, J.-S.B. & Smalyukh, I. I. Static Hopf solitons and knotted emergent fields in solid-state noncentrosymmetric magnetic nanostructures. *Phys. Rev. Lett.* **121**, 187201. <https://doi.org/10.1103/PhysRevLett.121.187201> (2018).
- Liu, Y., Lake, R. K. & Zang, J. Binding a hopfion in a chiral magnet nanodisk. *Phys. Rev. B* **98**, 174437. <https://doi.org/10.1103/PhysRevB.98.174437> (2018).

43. Kent, N. et al. Creation and observation of Hopfions in magnetic multilayer systems. *Nat. Commun.* **12**, 1562. <https://doi.org/10.1038/s41467-021-21846-5> (2021).
44. Liu, Y., Watanabe, H. & Nagaosa, N. Emergent magnetomultipoles and nonlinear responses of a magnetic hopfion. *Phys. Rev. Lett.* **129**, 267201. <https://doi.org/10.1103/PhysRevLett.129.267201> (2022).
45. Rybakov, F. N. et al. Magnetic hopfions in solids. *APL Mater.* **10**, 111113. <https://doi.org/10.1063/5.0099942> (2022).
46. Yu, X. et al. Realization and current-driven dynamics of fractional hopfions and their ensembles in a helimagnet FeGe. *Adv. Mater.* **35**, 2210646. <https://doi.org/10.1002/adma.202210646> (2023).
47. Guslienko, K. Magnetic hopfions: A review. *Magnetism* **4**, 383–399. <https://doi.org/10.3390/magnetism4040025> (2024).
48. Knapman, R., Tausendpfund, T., Diaz, S. A. & Everschor-Sitte, K. Spacetime magnetic hopfions from internal excitations and braiding of skyrmions. *Commun. Phys.* **7**, 1–9. <https://doi.org/10.1038/s42005-024-01628-3> (2024).
49. Azhar, M., Shaju, S. C., Knapman, R., Pignedoli, A. & Everschor-Sitte, K. 3D magnetic textures with mixed topology: Unlocking the tunable Hopf index. [arXiv:2411.06929](https://arxiv.org/abs/2411.06929)<https://doi.org/10.48550/arXiv.2411.06929> (2024).
50. Zheng, F. et al. Hopfion rings in a cubic chiral magnet. *Nature (London)* **623**, 718–723. <https://doi.org/10.1038/s41586-023-06658-5> (2023).
51. Wang, L. et al. Construction of a room-temperature Pt/Co/Ta multilayer film with ultrahigh-density skyrmions for memory application. *ACS Appl. Mater. Interf.* **11**, 12098–12104. <https://doi.org/10.1021/acsami.9b00155> (2019).
52. Liu, Y., Hou, W., Han, X. & Zang, J. Three-dimensional dynamics of a magnetic hopfion driven by spin transfer torque. *Phys. Rev. Lett.* **124**, 127204. <https://doi.org/10.1103/PhysRevLett.124.127204> (2020).
53. Raftrey, D. & Fischer, P. Field-driven dynamics of magnetic hopfions. *Phys. Rev. Lett.* **127**, 257201. <https://doi.org/10.1103/PhysRevLett.127.257201> (2021).
54. Müller, G. P., Rybakov, F. N., Jónsson, H., Blügel, S. & Kiselev, N. S. Coupled quasimonopoles in chiral magnets. *Phys. Rev. B* **101**, 184405. <https://doi.org/10.1103/PhysRevB.101.184405> (2020).
55. Shimizu, K., Okumura, S., Kato, Y. & Motome, Y. Current-induced motion of nanoscale magnetic torons over the wide range of the Hall angle. [arXiv:2407.02983](https://arxiv.org/abs/2407.02983)<https://doi.org/10.48550/arXiv.2407.02983> (2024).
56. Amaral, G. N. C. et al. Liquid crystal torons in Poiseuille-like flows. *Sci. Rep.* **15**, 2684. <https://doi.org/10.1038/s41598-024-83294-7> (2025).
57. Evans, R. F. L. Atomistic spin dynamics. In *Handbook of Materials Modeling: Applications: Current and Emerging Materials* (Andreoni, W. & Yip, S. eds.), 1–23. https://doi.org/10.1007/978-3-319-50257-1_147-1 (Springer, 2018).
58. Iwasaki, J., Mochizuki, M. & Nagaosa, N. Universal current-velocity relation of skyrmion motion in chiral magnets. *Nat. Commun.* **4**, 1463. <https://doi.org/10.1038/ncomms2442> (2013).
59. Wang, X. S., Qaiumzadeh, A. & Brataas, A. Current-driven dynamics of magnetic hopfions. *Phys. Rev. Lett.* **123**, 147203. <https://doi.org/10.1103/PhysRevLett.123.147203> (2019).
60. Seki, S. & Mochizuki, M. *Skyrmions in Magnetic Materials* (Springer, 2016).
61. Gilbert, T. L. A phenomenological theory of damping in ferromagnetic materials. *IEEE Trans. Mag.* **40**, 3443–3449. <https://doi.org/10.1109/TMAG.2004.836740> (2004).
62. Li, B. & Kovalev, A. A. Magnon Landau levels and spin responses in antiferromagnets. *Phys. Rev. Lett.* **125**, 257201. <https://doi.org/10.1103/PhysRevLett.125.257201> (2020).
63. Reichhardt, C. & Reichhardt, C. J. O. Depinning and nonequilibrium dynamic phases of particle assemblies driven over random and ordered substrates: A review. *Rep. Prog. Phys.* **80**, 026501. <https://doi.org/10.1088/1361-6633/80/2/026501> (2017).
64. Koshibae, W. & Nagaosa, N. Dynamics of skyrmion in disordered chiral magnet of thin film form. *Sci. Rep.* **9**, 5111. <https://doi.org/10.1038/s41598-019-41441-5> (2019).
65. Ester, M., Kriegel, H.-P., Sander, J. & Xu, X. A density-based algorithm for discovering clusters in large spatial databases with noise. *Proc. Second Int. Conf. Knowl. Discov. Data Min.* **34**, 226–231 (1996).
66. Lee, C.-S., Jankó, B., Derényi, I. & Barabási, A.-L. Reducing vortex density in superconductors using the ‘ratchet effect’. *Nature (London)* **400**, 337–340. <https://doi.org/10.1038/22485> (1999).
67. Villegas, J. E., Gonzalez, E. M., Sefrioui, Z., Santamaria, J. & Vicent, J. L. Vortex phases in superconducting nb thin films with periodic pinning. *Phys. Rev. B* **72**, 174512. <https://doi.org/10.1103/PhysRevB.72.174512> (2005).
68. de Souza Silva, C. C., Van de Vondel, J., Zhu, B. Y., Morelle, M. & Moshchalkov, V. V. Vortex ratchet effects in films with a periodic array of antidots. *Phys. Rev. B* **73**, 014507. <https://doi.org/10.1103/PhysRevB.73.014507> (2006).
69. Yu, K. et al. Asymmetric weak-pinning superconducting channels: Vortex ratchets. *Phys. Rev. B* **76**, 220507. <https://doi.org/10.1103/PhysRevB.76.220507> (2007).
70. Luo, M.-B. & Hu, X. Depinning and creep motion in glass states of flux lines. *Phys. Rev. Lett.* **98**, 267002. <https://doi.org/10.1103/PhysRevLett.98.267002> (2007).
71. Perez de Lara, D. et al. Vortex ratchet reversal: Role of interstitial vortices. *Phys. Rev. B* **83**, 174507. <https://doi.org/10.1103/PhysRevB.83.174507> (2011).
72. Reichhardt, C., Ray, D. & Reichhardt, C. J. O. Quantized transport for a skyrmion moving on a two-dimensional periodic substrate. *Phys. Rev. B* **91**, 104426. <https://doi.org/10.1103/PhysRevB.91.104426> (2015).

Acknowledgements

This work was supported by the US Department of Energy through Los Alamos National Laboratory. Los Alamos National Laboratory is operated by Triad National Security, LLC, for the National Nuclear Security Administration of the U. S. Department of Energy (Contract No. 892333218NCA000001). J.C.B.S and N.P.V. acknowledge funding from Fundação de Amparo à Pesquisa do Estado de São Paulo - FAPESP (Grants J.C.B.S 2023/17545-1 and 2022/14053-8, N.P.V 2024/13248-5). We would like to thank FAPESP for providing the computational resources used in this work (Grant: 2024/02941-1).

Author contributions

J.C.B.S. performed the investigation, figures and software, C.J.O.R., C.R. and A.S. wrote the manuscript and conceptualized the project, N.P.V. and P.A.V. provided funding. All authors reviewed the manuscript.

Declarations

The authors declare no competing interests.

Competing interests

The authors declare no competing interests.

Additional information

Supplementary Information The online version contains supplementary material available at <https://doi.org/10.1038/s41598-025-01349-9>

[0.1038/s41598-025-01349-9](https://doi.org/10.1038/s41598-025-01349-9).

Correspondence and requests for materials should be addressed to J.C.B.S.

Reprints and permissions information is available at www.nature.com/reprints.

Publisher's note Springer Nature remains neutral with regard to jurisdictional claims in published maps and institutional affiliations.

Open Access This article is licensed under a Creative Commons Attribution-NonCommercial-NoDerivatives 4.0 International License, which permits any non-commercial use, sharing, distribution and reproduction in any medium or format, as long as you give appropriate credit to the original author(s) and the source, provide a link to the Creative Commons licence, and indicate if you modified the licensed material. You do not have permission under this licence to share adapted material derived from this article or parts of it. The images or other third party material in this article are included in the article's Creative Commons licence, unless indicated otherwise in a credit line to the material. If material is not included in the article's Creative Commons licence and your intended use is not permitted by statutory regulation or exceeds the permitted use, you will need to obtain permission directly from the copyright holder. To view a copy of this licence, visit <http://creativecommons.org/licenses/by-nc-nd/4.0/>.

© The Author(s) 2025